PAPER

CrossMark
click for updates

Zinc-diffused silver indium selenide quantum dot sensitized solar cells with enhanced photoconversion efficiency†

Ganga Halder and Sayan Bhattacharyya*

Alloying of quantum dots (QDs) with suitable metal ions is one of the efficient tools to enhance the power conversion efficiency (PCE) of QD sensitized solar cells (QDSSCs). Ternary $AgInX_2$ (X = S, Se) based liquid-junction QDSSCs have low PCEs due to the presence of defect states at internal atom vacancies. However, Zn^{2+} diffusion at these vacant sites can improve the carrier mobility of the QDs. The QDSSCs with Zn^{2+}-diffused $AgInSe_2$ (ZAISE) QDs have a broad light harvesting range up to the near-infrared (NIR) range. PCE was enhanced from a merely 1.67% for pristine $AgInSe_2$ QDs (AISE) to 3.07% for ZAISE with a Zn/(Ag + In) ratio of 48.2%, aided by an optimized ZnS passivation layer on the photoanode. The device efficiency was further improved to 3.57% by applying dual passivation of amorphous TiO_2 and SiO_2 layers. This approach could effectively suppress the recombination pathways at the QD surface and thereby minimize back electron transfer from photoexcited electrons of QDs and from the conduction band of TiO_2 to the polysulfide electrolyte. The combined strategy of alloying with Zn^{2+} and inorganic passivation could achieve the highest ever PCE of environmentally friendly $AgInX_2$ based QDSSCs.

1. Introduction

Semiconductor QDs have size-controllable photophysical properties such as the tunability of their band gap, a high absorption coefficient, an ability to generate multiple excitons by a single photon and a large carrier lifetime which offers the possibility of boosting the PCE of photovoltaic devices beyond the Shockley–Queisser limit.[1–5] In QDSSCs, narrow band gap cadmium and lead based chalcogenide semiconductors like CdS, CdSe, PbS, and PbSe are popularly employed as sensitizers and wider band gap metal oxide semiconductors like TiO_2, ZnO and SnO_2 are used as electron acceptors.[6] However, the low to moderate PCE of these binary QDs lingers due to their limited light harvesting range and/or poor charge injection efficiency. In comparison, alloyed QDs are superior substitutes since their band gap can be tuned by changing their composition to obtain a broad light harvesting range and suitable band gap alignment for effective charge injection.[7] Recently, copper and silver based ternary QDs have received attention for the fabrication of third generation photovoltaic devices due to their broad light harvesting range from the UV-visible to the NIR region. This broad range is very crucial for capturing a large number of solar photons. More importantly, these ternary alloyed QDs are free from toxic elements such as cadmium and lead which will open a new window for the commercial application of "non-toxic" QDs in QDSSCs for future environmental prospects.[8–10]

Although ternary alloyed QDs are good light harvesters, the efficiency of the photovoltaic devices is limited due to their high density of trap states which act as recombination centers in QDSSCs.[10–12] $AgInSe_2$ (AISE) is a I-III-VI$_2$ semiconductor having a direct bulk band gap of 1.19 eV, which is ideal for solar cell applications attributed to its high absorption coefficient. Although it has a broad light harvesting range, several vacancies at Ag and Se lattice sites along with internal atom vacancies lead to defect states.[13,14] In order to improve the PCE, silver chalcogenides were manipulated through creation of Ag_2S–$AgInS_2$ based p–n junction heterostructures[15,16] and $AgInS_2$ QDs/In_2S_3 based photoelectrodes,[17] or introducing a buffer layer between $AgInS_2$ QD sensitizers and ZnO nanorod arrays.[18] In spite of several efforts, the device efficiency is still low. The presence of defect states reduces the crystallinity, electrical conductivity and carrier mobility in ternary QDs. These trap states with a high density also act as recombination centers, thereby decreasing the photovoltage and photovoltaic performance.[19,20] One of the ways to reduce the density of surface trap states is surface modification of ternary QDs where the passivation layers act as a barrier to minimize the electron and hole transfer rates.[8,9,21]

The diffusion of foreign metal ions into the vacant sites of ternary QD lattices is another suitable approach to improve the

Department of Chemical Sciences and Centre for Advanced Functional Materials, Indian Institute of Science Education and Research (IISER) Kolkata, Mohanpur-741246, India. E-mail: sayanb@iiserkol.ac.in

† Electronic supplementary information (ESI) available: Powder XRD pattern of Ag_2Se; Tauc plots; PL spectra of AZ4 and AZ6 QDs synthesized at different temperatures; *J*–*V* characteristics and variation of Nyquist plots, R_{rec} and C_μ as a function of the bias voltage of AZ5 QDSSCs with different ZnS SILAR cycles. See DOI: 10.1039/c7ta00268h

11746 | *J. Mater. Chem. A*, 2017, **5**, 11746–11755

This journal is © The Royal Society of Chemistry 2017

conductivity as well as PCE by minimizing the prevalent defect states. For example, Cu-diffused AISE QDs in organic/inorganic bulk-heterojunction devices decrease the internal resistance and increase the short-circuit current density (J_{SC}) under white light illumination.[22] These alloying strategies alter the energy difference (ΔE_{CB}) between the conduction energy levels of the QDs and metal oxide, henceforth increasing the injection efficiency of the photogenerated electrons. If ΔE_{CB} is large enough, then photogenerated electrons can be rapidly injected into the metal oxide to enhance the charge collection efficiency and PCE.[23] Although QDSSCs with ternary alloyed Zn–CuInSe$_2$ QD sensitizers have already achieved 11.6% PCE through manipulation of the conduction band energy level,[24] the breakthrough in AISE QD sensitized QDSSCs is much in demand to achieve improved PCE by increasing the crystallinity and carrier mobility of the QDs as well as by applying appropriate surface passivation.

In this work, Zn^{2+}-diffused $AgInSe_2$ (ZAISE) QDs with a broad light harvesting range from visible to NIR were synthesized by a hot injection method. The chemical composition of the QDs was varied by altering the ratio of Zn/(Ag + In). Higher Zn diffusion increases the ZAISE band gap. Through different optimization steps, the best PCE obtained is 3.57% when the Zn/(Ag + In) at% is 48.2. Our strategy could enhance the PCE of these "non-toxic" QDSSCs by ~23% as compared to previous attempts.

2. Results and discussion

2.1 Characterization of the QDs

2.1.1 Structural characterization. A two-step in one pot synthetic procedure was employed for the preparation of ZAISE QDs. In the first step, the Ag$_2$Se QDs were synthesized within 3 min at 88 °C from the reaction between Ag-oleylamine complex solution with very reactive phosphine-free Se-precursor. The Se-precursor was obtained from the reduction of Se powder by a 1 : 1 mixture of oleylamine and dodecanethiol. The Ag$_2$Se QDs crystallize in the orthorhombic crystal structure according to JCPDS pattern 24-1041 (Fig. S1†). Thereafter the reaction mixture was further heated to 180 °C for the diffusion of In^{3+} and Zn^{2+} into the Ag$_2$Se crystal lattice to form ZAISE QDs. Since the ionic radii of In^{3+} and Zn^{2+} are 1.44 and 0.68 Å, respectively, these ions can easily diffuse into the vacant sites of Ag$_2$Se where the ionic radius of Ag^+ is 1.54 Å.[25,26] The QD samples denoted as AZ0, AZ4, AZ5 and AZ6 have a Zn:(Ag + In) at% of 0, 36, 48 and 58, respectively, as obtained by inductively coupled plasma mass spectrometry (ICP-MS) analyses. The powder X-ray diffraction (XRD) patterns in Fig. 1a show that all the QDs crystallize in the tetragonal crystal structure (Fig. 1b) with space group $\bar{I}42d$ according to the JCPDS pattern 75-0118. ICP-MS data show that on moving from AZ0 to AZ5, the drop in Ag:(Ag + In + Zn) is 30% whereas that of In:(Ag + In + Zn) is 70%. Therefore it is evident that a majority of Zn^{2+} sits in the In^{3+} sites than at Ag^+ sites, and the relatively closer ionic radii of In^{3+} and Zn^{2+} are another validation to this argument. Also, the simultaneous diffusion of In^{3+} and Zn^{2+} in the Ag$_2$Se lattice provides a competition between them to occupy the lattice vacancies. The crystallite size of the QDs is 3.2–3.5 nm which is

calculated from the powder XRD pattern of the QDs using the Debye–Scherrer equation after subtracting the instrumental broadening. The representative transmission electron micrographs (TEMs) show that the particle size of the monodisperse QDs is around 4–6 nm with a moderately narrow size distribution (Fig. 1c and e). The AISE and ZAISE QDs were ligand-exchanged by replacing the initial hydrophobic oleylamine surfactant with mercaptopropionic acid (MPA) in order to obtain a maximum loading of the QDs on the TiO$_2$ substrate and improve the film conductivity of QDSSCs.[27] The interplanar spacing shows the high crystallinity and the indexed fast Fourier transform (FFT) patterns (Fig. 1d and f) confirm the purity of the as-synthesized QDs.

2.1.2 Optical characterization. The absorption spectra of all the QDs synthesized at 180 °C (Fig. 2a and S2†) show a broad light harvesting range from visible to NIR, an essential requirement to achieve high efficiency QDSSCs. The band gap of AZ0, AZ4, AZ5 and AZ6 is 1.50, 1.50, 1.53, and 1.56 eV as measured from the Tauc plots (Fig. S3a†). To evaluate the
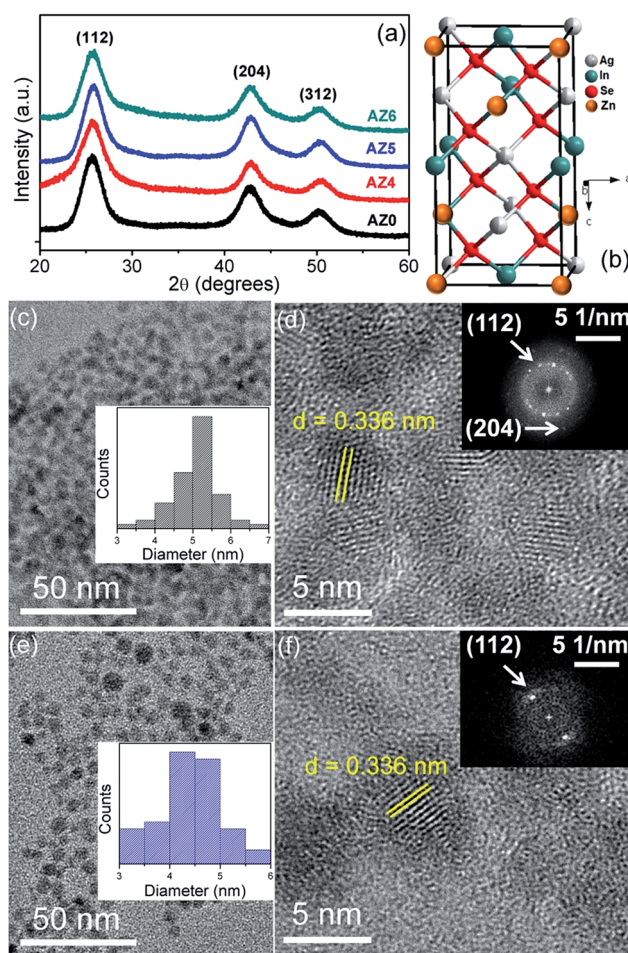

Fig. 1 (a) Powder XRD patterns of the QDs. (b) Representative unit cell of AZ5. (c) Low resolution TEM image of AZ0 with the diameter histogram as the inset. (d) High resolution TEM image of AZ0 with the FFT pattern as the inset. (e) Low resolution TEM image of AZ5 with the diameter histogram as the inset. (f) High resolution TEM image of AZ5 with the FFT pattern as the inset.

This journal is © The Royal Society of Chemistry 2017

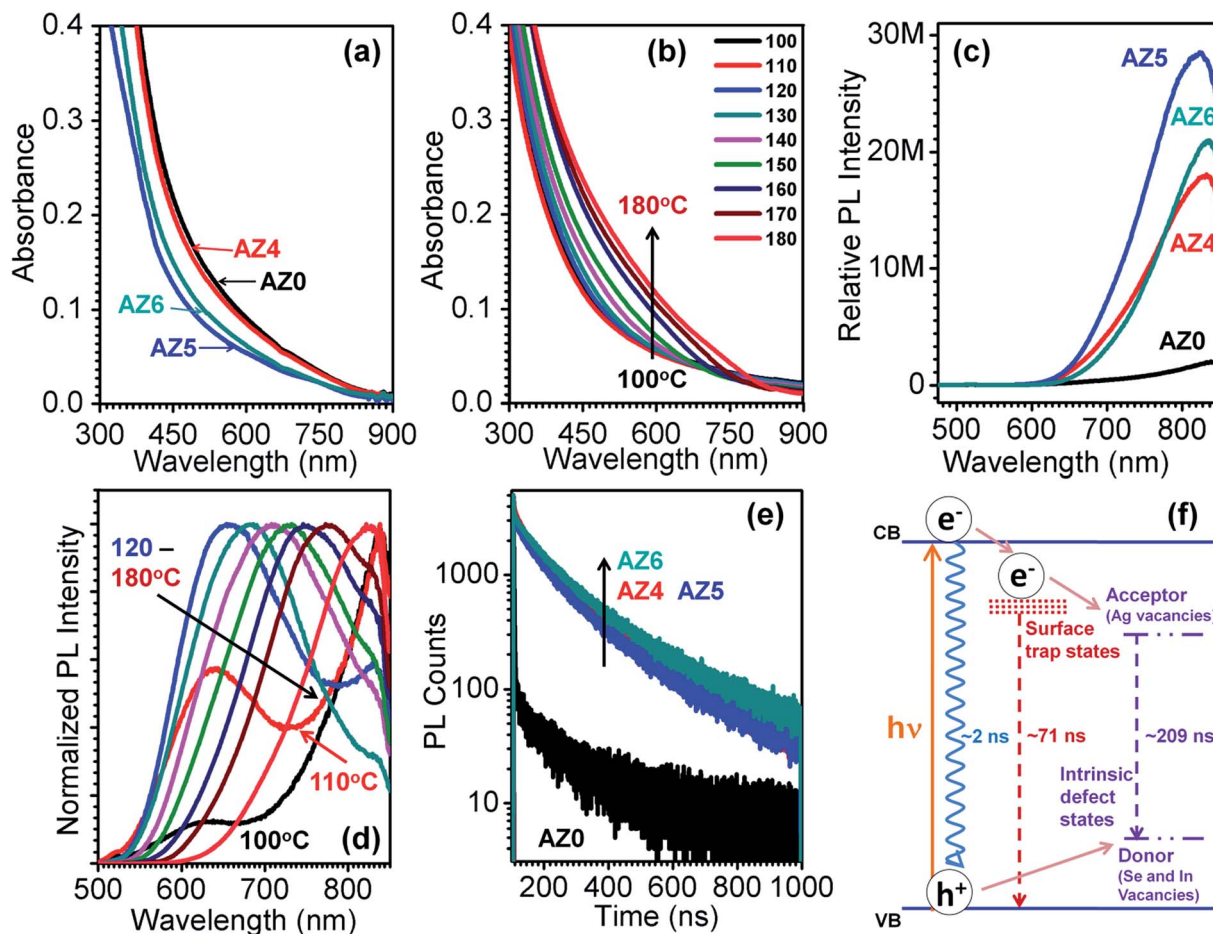J. Mater. Chem. A, 2017, 5, 11746–11755 | 11747

Fig. 2 (a) Absorption spectra of the colloidal QDs synthesized at 180 °C. (b) Reaction temperature dependent absorption spectra of AZ5 QDs. (c) Relative PL intensity plot of the QDs. (d) Reaction temperature dependent PL spectra of AZ5 QDs. Excitation wavelength: $\lambda_{ex} = 450$ nm. (e) PL lifetime decay plots of colloidal QDs. All spectra were recorded in chloroform. (f) Schematic energy level diagram (not to scale) showing the recombination pathways.

impact of synthesis temperature and resultant particle size on the band gap, the absorption spectra of AZ5 QDs were recorded with the aliquots at different reaction temperatures. Fig. 2b shows the reaction temperature dependent UV-Vis-NIR spectra of AZ5 QDs. Due to the increase of the particle size at higher temperatures, the light harvesting range becomes broader. As a result the band gap decreases from 2 eV at 100 °C to 1.53 eV at 180 °C (Fig. S3b†). Among the AZ0–AZ6 QDs synthesized at 180 °C, AZ5 shows the maximum photoluminescence (PL) intensity (Fig. 2c). With higher incorporation of Zn^{2+} ions, the peak position is slightly blue shifted from AZ0 to AZ6 QDs.[28] The room temperature emission spectra of AZ5 QDs were also recorded by taking the aliquots at different reaction temperatures (Fig. 2d). Two distinct emission bands are observed with QDs from aliquots at 100 and 110 °C. The band at higher wavelengths can be attributed to the emission from cation vacancy defects, since at 100–110 °C, Zn^{2+} ions have minimum probability to enter the vacant sites. The emission band at lower wavelengths arises from donor–acceptor pair recombination within the band gap with Ag^+ vacancies as the acceptor, and Se^{2-} and In^{3+} vacancies as donors (Fig. 2d).[29] The intensity of the lower wavelength band gradually increases with an increase

in the reaction temperature which indicates higher incorporation of Zn^{2+} and In^{3+} into the vacant sites of Ag_2Se.[14,28,30] At elevated temperatures, these two bands merge into a broad intense emission band. This broad emission band (full width at half maxima >100 nm) is an indication of the formation of alloyed QDs.[30] The peak maximum is gradually red shifted due to the faster growth of QDs at higher temperatures. The reaction temperature dependent PL spectra of AZ4 and AZ6 QDs (Fig. S4†) show a similar trend to that of AZ5.

Fig. 2e shows the fluorescence decay curves of all the QDs at an excitation wavelength of 402 nm. The PL decay was recorded at 840, 834, 832 and 830 nm for AZ0, AZ4, AZ5 and AZ6 QDs, respectively. The PL decay profiles are found to be tri-exponential with an average lifetime of 232.7, 180.1, 184.8 and 203.9 ns for AZ0, AZ4, AZ5 and AZ6 QDs, respectively (Table 1). Fig. 2f provides the schematic energy level diagram showing the three recombination pathways with different lifetimes (τ) and their amplitude (A). The faster decay component ($\tau_3 \sim 2$ ns) arises due to non-radiative processes e.g. Auger recombination and its contribution (A_3) is the highest in AZ0. In AZ4 to AZ6, the contribution of this component is dominated by surface trap state emission ($\tau_1 \sim 66.6$–75.6 ns) and donor–acceptor

11748 | J. Mater. Chem. A, 2017, 5, 11746–11755

This journal is © The Royal Society of Chemistry 2017

Table 1 PL lifetime decay parameters of QDs synthesized at 180 °C

QD code	A_1	τ_1 (ns)	A_2	τ_2 (ns)	A_3	τ_3 (ns)	χ^2	$\langle\tau\rangle$ (ns)
AZ0	12.68	37.7	53.15	240.8	34.17	1.33	1.13	232.7
AZ4	29.49	66.6	69.65	196.4	0.85	2.67	1.04	180.1
AZ5	30.68	67.9	68.23	202.5	1.09	1.69	1.09	184.8
AZ6	29.08	75.6	70.07	222.1	0.85	1.94	1.06	203.9

recombination ($\tau_3 \sim$ 196.4–222.1 ns) between the Ag$^+$ vacancies as donor sites and In^{3+} and Se^{2-} vacancies as acceptor sites.[31] In the absence of Zn^{2+} (AZ0) the contributions from surface trap state emission and donor–acceptor recombination to the total average lifetime are lower as compared to those of AZ4–AZ6. Since τ_2 increases from 196.4 ns to 222.1 ns for AZ4 to AZ6 QDs, respectively, it is evident that Zn^{2+} diffusion in the In^{3+} and Ag$^+$ sites allows lesser donor–acceptor recombination. However, the contribution of surface trap state emission (A_1) increases from 12.7 for AZ0 to 29.1–30.7 for AZ4–AZ6. The variation of τ_1 and A_1 implies that Zn^{2+} ions occupy surface sites till saturation before diffusing to the vacancy sites inside the AgInSe$_2$ lattice. This is manifested from similar band gaps of AZ0 and AZ4, before increasing for AZ5 and AZ6 by Zn^{2+} lattice diffusion. In this case, segregation of a separate ZnSe phase at the QD surface is possible; however no such evidence is obtained from the XRD patterns in Fig. 1a.
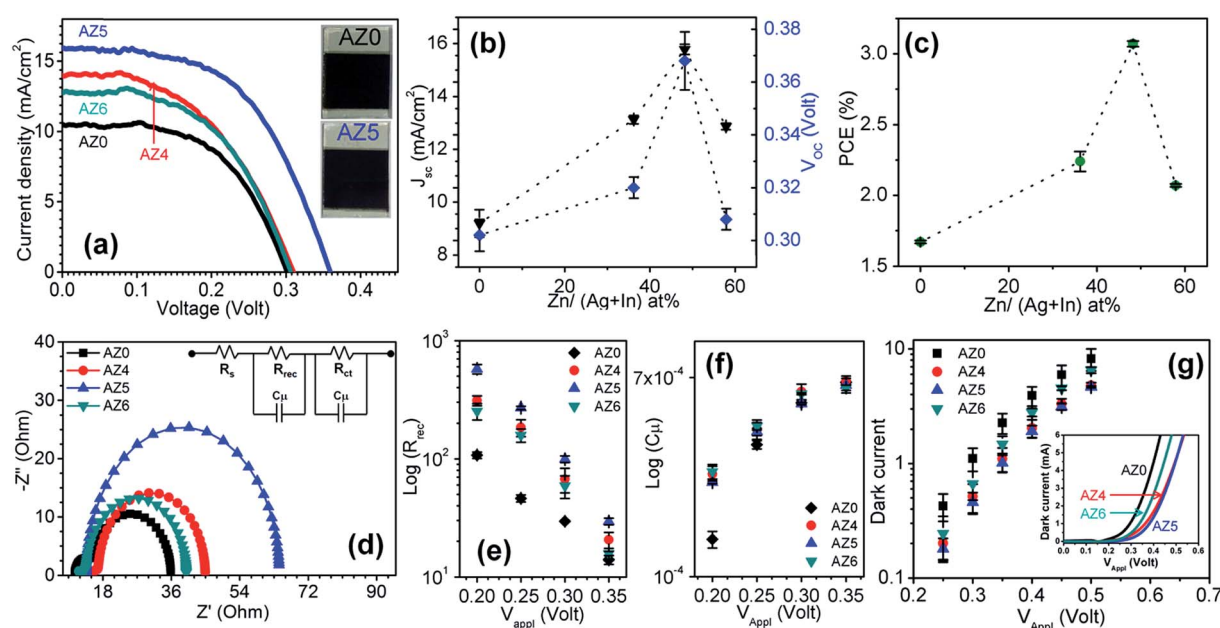
2.2 Photovoltaic performance of the QDs

The working electrodes were prepared by dip coating of the as-prepared ~9 μm thick TiO$_2$ films on fluorine-doped tin oxide (FTO) coated glass substrates in aqueous dispersions of MPA-

capped QDs. With the counter electrode made of a paste of microwave synthesized CuS powder[32] and the sandwiched droplet of the electrolyte between the working and counter electrodes, at first the performance of AZ0–AZ6 based QDSSCs was tested. Here 8 cycles of ZnS passivation layers were applied on the working electrode by successive ionic layer adsorption and reaction (SILAR). Second, the number of ZnS SILAR cycles was optimized with the best performing QDs. In the third step, a double inorganic passivation of amorphous TiO$_2$ and SiO$_2$ was applied to further enhance the photovoltaic performance. Electrochemical impedance spectroscopy (EIS) was used to explain the trends and the role of passivation.

2.2.1 Performance of AISE and ZAISE QDSSCs. The current density (J)–voltage (V) characteristics of the QDSSCs fabricated with AZ0–AZ6 QDs are shown in Fig. 3a. The open circuit voltage (V_{OC}), J_{SC}, fill factor (FF) and PCE (η%) of the QDSSCs are tabulated in Table 2 where 8 ZnS SILAR cycles were applied in all the QDSSCs. The variation of all the solar cell parameters is shown in Fig. 3b and c as a function of Zn/(Ag + In) at%. V_{OC} increases from 0.30 V for AZ0 to 0.37 V for AZ5 films and decreases for AZ6. The photocurrent also shows a similar trend where the highest J_{SC} is observed for AZ5 (15.78 mA cm^{-2}) as compared to AZ0 (9.91 mA cm^{-2}). The photovoltaic performance was observed to be the highest for AZ5 QDSSCs (3.07%) which is 45.6% more than that of AZ0 QDSSCs (1.67%).

The EIS measurements were carried out in the dark to highlight the significant improvement of the device efficiency upon zinc incorporation into the QDs.[33] Fig. 3d shows the Nyquist plots recorded in the frequency range from 0.1 Hz to 1 MHz at a forward bias of −0.35 V, which is very close to the V_{OC} of the QDSSCs. The Nyquist plots are fitted with an equivalent

Fig. 3 (a) J–V characteristics of the QDSSCs under 1 sun illumination. (Inset) Digital images of AZ0 and AZ5 photoanodes. Variation of the (b) J_{SC} and V_{OC}, and (c) PCE of the QDSSCs as a function of Zn/(Ag + In) at%. (d) Nyquist plot of the QDSSCs at −0.35 V forward bias under dark conditions with the equivalent circuit as the inset. Plots of the (e) recombination resistance and (f) chemical capacitance of the QDSSCs with applied potential. (g) Variation of dark current with applied potential in the log scale (inset shows the normal scale).

This journal is © The Royal Society of Chemistry 2017

J. Mater. Chem. A, 2017, **5**, 11746–11755 | **11749**

Table 2 QDSSC parameters after treatment of 8 ZnS cycles by SILAR

QDSSCs	Zn/(Ag + In) at%	J_{SC} (mA cm^{-2})	V_{OC} (V)	FF	η^a (%)
AZ0	0	9.91 ± 0.54	0.302 ± 0.004	0.555 ± 0.006	1.67 ± 0.10
AZ4	36.2	13.13 ± 0.16	0.320 ± 0.004	0.526 ± 0.013	2.24 ± 0.07
AZ5	48.2	15.78 ± 0.19	0.368 ± 0.011	0.529 ± 0.013	3.07 ± 0.02
AZ6	57.9	12.87 ± 0.13	0.308 ± 0.004	0.520 ± 0.007	2.07 ± 0.01

[a] Average of three cells in parallel.

circuit as shown in the Fig. 3d inset. All the EIS parameters *e.g.* series resistance (R_s), charge recombination resistance at photoanode and electrolyte interfaces (R_{rec}), and chemical capacitance (C_μ) are tabulated in Table 3. No significant change of R_s is observed for different QDSSCs since it depends upon the transport resistance of FTO and the connection setup which is equivalent for all the measurements. However, a considerably higher R_{rec} is observed in ZAISE than AISE QDSSCs (Fig. 3e). Since R_{rec} is inversely proportional to the charge recombination rate, the latter becomes sluggish at the interface of the ZAISE photoanode and the electrolyte than with the AISE photoanode. The photovoltaic data shown in Table 2 can be directly correlated with R_{rec} data which shows the significant improvement of the efficiency of ZAISE based devices. The C_μ of all the QDSSCs is similar at different applied voltages (Fig. 3f), due to the unchanged TiO$_2$ conduction band position with different QD sensitizers. As a cross-check on the recombination rate in QDSSCs, their *I–V* characteristics were also measured in the dark (Fig. 3g inset) and the dark or recombination current is plotted as a function of applied voltage (Fig. 3g). The dark current in ZAISE QDSSCs is less than that in AISE QDSSCs at the same applied voltage which further proves the slower charge recombination at the photoanode/electrolyte interfaces in ZAISE QDSSCs.

The relatively higher efficiency of AZ5 QDSSCs even though the average lifetime of AZ5 colloidal QDs is lower than those of AZ0 and AZ6 is quite intriguing (Table 1). When the QD surface layer is passivated by 8 ZnS SILAR cycles, the surface trap state recombination is reduced. Since AZ5 has a relatively higher contribution of τ_1, the QDSSCs with AZ5 QDs are mostly benefitted. Interestingly in this work, a total of 8 ZnS SILAR cycles are required to make a well passivated layer on the QD surface whereas there are reports where 4 ZnS SILAR cycles are employed to achieve the highest device efficiency.[2,34,35] This clearly highlights the importance of reducing the surface trap

state emission. The surface passivation however cannot alter the τ_2 and τ_3 components *i.e.* non-radiative and donor–acceptor recombination processes which are inherent to the QDs with a specific Zn^{2+} concentration. Due to the reduction in surface trap states, slower charge recombination occurs at the TiO$_2$/QD/electrolyte interface which increases the PCE of AZ5-8Z QDSSCs. On the other hand, due to a large amount of non-radiative loss, PCE is the least for AZ0-8Z QDSSCs (Table 2).

2.2.2 Variation of ZnS SILAR cycles. To probe the extent of passivation, the number of the ZnS SILAR cycles was varied and applied onto the AZ5-fabricated QDSSCs. The cells are denoted as AZ5-4Z, AZ5-8Z and AZ5-10Z for 4, 8 and 10 ZnS SILAR cycles, respectively. The photocurrent increases by 31.2% from AZ5-4Z to AZ5-8Z (Table S1†) due to surface passivation of unsaturated dangling bonds and surface trap states of the QDs. V_{OC} also increases from 0.34 V for AZ5-4Z to 0.37 V for AZ5-8Z whereas FF also shows a similar trend. From AZ5-8Z to AZ5-10Z, although J_{SC} and FF remain almost constant, V_{OC} decreases. Thus, the overall PCE is the highest with 8 ZnS cycles (Fig. S5†). R_{rec} is significantly higher for AZ5-8Z and AZ5-10Z compared to AZ5-4Z. However C_μ is lower for AZ5-10Z at different applied voltages, a trend similar to an earlier report for CuInSe$_2$ QDSSCs with a higher number of ZnS cycles.[36] The deposition of passivation layers beyond the optimum thickness can partially block the TiO$_2$ pores leading to poor infiltration of the electrolyte.[2] 10 ZnS SILAR cycles can agglomerate the QDs which limits the interfacial contact between porous TiO$_2$ and the polysulfide electrolyte and therefore with a limiting charge injection propensity, PCE does not improve beyond that of AZ5-8Z. The blocking of pores may promote processes such as auger recombination or radiative recombination due to the presence of long lived holes in the ZAISE QDs and limited hole transfer from QDs to the electrolyte.[35]

2.2.3 Effect of TiO$_2$/SiO$_2$ double passivation. With the goal to improve the PCE beyond 3.07%, the photoanode containing 8

Table 3 EIS parameters of QDSSCs after different post treatment processes

QDSSCSs	R_s (Ω cm^{-2})	R_{rec} (Ω cm^{-2})	C_μ (mF cm^{-2})	f_{max} (Hz)	τ_n (ms)
AZ0-8Z	10.65	12.58	0.70	12.12	13.11
AZ4-8Z	15.34	17.06	0.64	8.25	19.26
AZ5-8Z	12.25	30.78	0.68	5.62	28.27
AZ6-8Z	11.88	15.98	0.62	10.00	15.90
AZ5-4Z	12.1	21.58	0.67	8.25	19.26
AZ5-10Z	14.8	27.61	0.63	6.81	23.34
AZ5-8ZTS	12.75	46.87	0.65	3.83	41.50

11750 | *J. Mater. Chem. A*, 2017, **5**, 11746–11755

This journal is © The Royal Society of Chemistry 2017

ZnS SILAR cycles was enriched with amorphous TiO$_2$ and SiO$_2$ passivation layers to make AZ5-8ZTS cells. These double passivation layers increase both J_{SC} and V_{OC} as shown in Fig. 4a and tabulated in Table 4. A very significant change in FF is observed from 0.53 for AZ5-8Z to 0.59 for AZ5-8ZTS. By following these techniques, the best PCE of 3.57% is achieved for AZ5-8ZTS QDSSCs which is 15.9% higher than that of AZ5-8Z QDSSC. Likewise the charge recombination is also reduced as shown in Fig. 4b and c. Although R_{rec} does not improve from 8 to 10 ZnS cycles, a very thin SiO$_2$ layer on top of 8 cycles of ZnS can slow down the recombination rate by saturating the dangling bonds through Ti–S and Zn–O bond formation without any change in C_μ (Fig. 4d). The lifetime of the electrons (τ_n) is calculated from the Bode plot (Fig. 4e) by using eqn (1):

$$\tau_n = 1/(2\pi f_{max}) \tag{1}$$

where f_{max} is the frequency maxima of the lower frequency peak in the Bode plot. The calculated lifetime of AZ0-8Z, AZ5-8Z and AZ5-8ZST QDSSCs is 13.1, 28.3 and 41.5 ms, respectively (Table 3). This higher recombination lifetime of the electrons further confirms the slower charge recombination processes after applying amorphous TiO$_2$ on top of the QD layer and SiO$_2$ on the ZnS layer. This result is further supported by the dark current measurements at different applied voltages (Fig. 4f).

Several charge recombination processes which are responsible for the low PCE of QDSSCs include band edge recombination between the valence band holes and the conduction band electrons in QDs, back electron transfer to the electrolyte

Table 4 QDSSC parameters for AZ0 and AZ5 after different post treatments

QDSSCs	J_{SC} (mA cm^{-2})	V_{OC} (V)	FF	η (%)
AZ0-8Z	9.91 ± 0.54	0.302 ± 0.004	0.555 ± 0.006	1.67 ± 0.10
AZ5-8Z	15.78 ± 0.19	0.368 ± 0.011	0.529 ± 0.013	3.07 ± 0.02
AZ5-8ZTS[a]	15.78 ± 0.23	0.378 ± 0.002	0.576 ± 0.016	3.41 ± 0.16
AZ5-8ZTS[b]	16.03	0.381	0.585	3.57

[a] Average of three cells in parallel. [b] Champion cell.

Fig. 5 Schematic of the AZ5-8ZTS based QDSSC showing the electron transfer (solid curved arrows) and recombination pathways (dotted straight arrows).
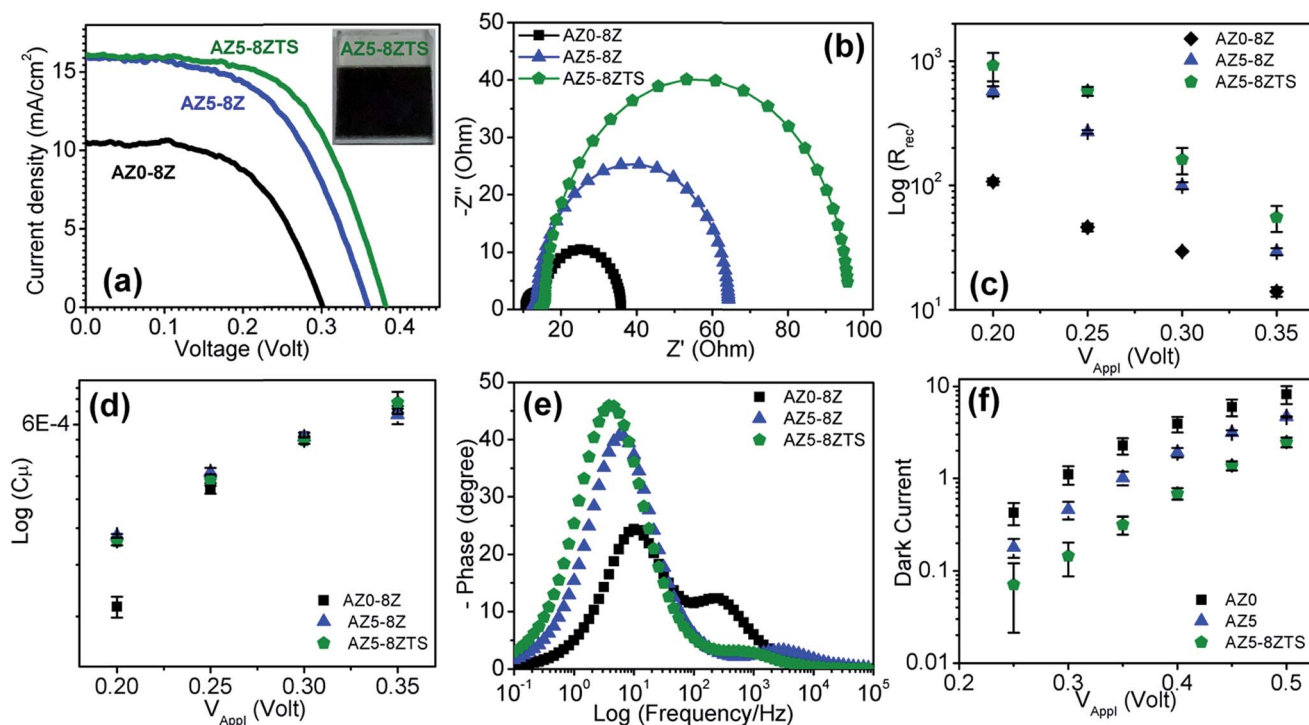

Fig. 4 (a) J–V characteristics of the representative QDSSCs under 1 sun illumination. (Inset) Digital image of the AZ5-8ZTS photoanode. (b) Nyquist plot of the QDSSCs at −0.35 V forward bias under dark conditions. Plots of the (c) recombination resistance and (d) chemical capacitance of the QDSSCs with applied potential. (e) Bode plots of the QDSSCs. (f) Variation of dark current with applied potential in the log scale.

Table 5 Review of literature reports on AgInS$_2$/Se$_2$ solar cells

QD	Synthesis method	Deposition method[b]	Nature of devices	PCE (%)	Ref.
Cu diffused AgInS$_2$	HI + HU[a]	Spin coating	Bulk heterojunction	1.13	22
ZnO/ZnS/AgInS$_2$ nanotube arrays	NA	Chemical etching + anion exchange + autoclave	Inorganic–organic hybrid solar cell	2.11	18
AgInS$_2$	Ligand-free synthesis	Direct deposition	Liquid junction	0.80	10
ZnSe-AgInSe$_2$/CdS	HU	SA + SILAR[b]	Liquid junction	1.90	43
Ag$_2$S/AgInS$_2$ heterostructures	HI	NA	Bulk heterojunction	0.52	15
Ag$_2$S/AgInS$_2$ nanoheterodimers	Thermolysis	Direct deposition	Liquid junction	1.30	16
AgInS$_2$/In$_2$S$_3$	NA	SILAR	Liquid junction	0.70	17
AgInS$_2$-ZnS	HI	EPD	Liquid junction	2.25	44
AgInS$_2$	HU	SA via ligand exchange	Liquid junction	2.9	45
Zn-AgInSe$_2$	HI + HU	SA via ligand exchange	Liquid junction	3.57	This work

[a] HI = hot-injection method; HU = heating-up method. [b] SA = self-assembly; EPD = electrophoretic deposition; NA = not available.

from photoexcited electrons of QDs and from the conduction band of TiO$_2$, recombination of conduction band electrons of TiO$_2$ with the valence band hole of QDs, and surface trapping of photoexcited electrons of QDs and conduction band electrons of TiO$_2$.[37] The modification of the photoanode surface with suitable inorganic and organic passivation layers is a key step to suppress these charge recombination pathways and improve the device efficiency.[38–40] Inorganic passivation can suppress a majority of these recombination pathways which indeed is the key step to enhance the PCE of QDSSCs.[34,41,42] In this work, when ZnS is deposited by SILAR onto the QD-coated TiO$_2$ substrate, it likely passivates the dangling bonds present on the TiO$_2$ surface through the formation of well-ordered Zn–O and S–Ti bonds. The amorphous TiO$_2$ coating, on the QD-deposited TiO$_2$ photoanode, acts as a buffer layer at the interface between TiO$_2$/QDs and ZnS/SiO$_2$ thus reducing the interfacial trap states to enhance the device efficiency. Further, the deposition of SiO$_2$ on ZnS can passivate all the exposed Zn and S surface atoms through the formation of Si–S and O–Zn bonds at the interface of ZnS and SiO$_2$.[35] The coating of these different inorganic passivation layers is evident in the TEM image of the photoanode (Fig. S6†). However, the separate layers could not be distinguished in the ~1.5 nm thick amorphous coating. The energy dispersive analysis of X-rays (EDAX) and elemental mapping in fact confirm the presence of Zn, S, O and Si elements.

To understand the role of passivation layers, QDs were deposited onto an insulating mesoporous SiO$_2$ layer on FTO glass. Since there will be no charge injection from the QDs into the SiO$_2$ layer, the changes in PL spectra (Fig. S7†) with different passivation layers can verify the significance of passivation. The PL intensity decreases by coating of an amorphous TiO$_2$ layer onto the QDs due to injection of charge from QDs into TiO$_2$. The PL intensity increases again by applying ZnS and SiO$_2$ coatings over the film due to surface passivation of the QDs. ZnS and TiO$_2$/SiO$_2$ passivation however will be able to control neither the band edge recombination in QDs, nor the recombination pathways between QDs and the TiO$_2$ photoanode which remain in contact without any interfacial layer. In fact these passivation layers at the interface of the photoanode and electrolyte potentially reduce or stop the

back electron transfer from photoexcited electrons of QDs and from the conduction band of TiO$_2$ to the electrolyte. A schematic is shown in Fig. 5 where the desired electron transfer pathways are shown by thicker curved arrows and the undesired recombination pathways are shown with dotted arrows. Overall, this strategic combination of alloying with Zn in AISE QDs, optimized ZnS layers and TiO$_2$/SiO$_2$ double passivation could significantly enhance the PCE of AISE based QDSSCs to 3.57%, which is ~23% higher than the best of previous reports (Table 5).[10,15–18,22,43–45]

3. Conclusions

Zn^{2+}-diffused AgInSe$_2$ QDs with a Zn:(Ag + In) at% of 36, 48 and 58 were synthesized by a hot-injection method and applied as light harvesters in QDSSCs. A majority of Zn^{2+} ions occupy the In^{3+} sites over Ag$^+$ sites. The QDs had a broad light harvesting range from the visible to the NIR region and the PL lifetime decreases with Zn^{2+}-diffusion up to a Zn:(Ag + In) at% of 48.2 (AZ5). The AISE and ZAISE QDs were ligand-exchanged with MPA to achieve a maximum loading of the QDs on the TiO$_2$ photoanode. Apart from improving the crystallinity and carrier mobility of the QDs, diffusion of Zn^{2+} also tunes the intrinsic band gap. With 8 SILAR cycles of ZnS on top of the QD-deposited TiO$_2$ photoanode the PCE was improved from 1.67% for AZ0 to 3.07% for AZ5. The passivation by ZnS reduces the surface trap state recombination whereas the non-radiative and donor–acceptor recombination processes likely remain unchanged. The PCE was further enhanced to 3.57% by dual inorganic passivation according to the TiO$_2$/QD/amorphous TiO$_2$/ZnS/SiO$_2$ configuration. In addition to the suppression of surface trap states, the surface passivation reduces the recombination pathways of back electron transfer from photoexcited electrons of QDs and also from the conduction band of TiO$_2$ to the polysulfide redox electrolyte. The record PCE of 3.57% is so far the highest achieved for ternary AgInX$_2$ (X = S, Se) based QDSSCs. A similar strategy coupled with a surface passivation approach is effective in enhancing the device efficiency of other low performing QD systems in photovoltaic applications.

11752 | J. Mater. Chem. A, 2017, 5, 11746–11755

This journal is © The Royal Society of Chemistry 2017

4. Experimental section

4.1 Materials

Silver nitrate (AgNO$_3$, Sigma Aldrich, 98%), indium chloride tetrahydrate (InCl$_3$·4H$_2$O, Sigma Aldrich, 99.999%), oleylamine (Sigma Aldrich, ≥98%), 1-octadecene (Sigma Aldrich, technical grade, 90%), 1-dodecanethiol (Sigma Aldrich, ≥98%), zinc acetate dihydrate Zn(OAc)$_2$·2H$_2$O (Merck India, 98%), zinc nitrate hexahydrate Zn(NO$_3$)$_2$·6H$_2$O (reagent grade, 98%), sulfur powder (purified, Merck India), sodium sulfide flakes (Na$_2$S·9H$_2$O, purified, Merck India), potassium chloride (purified, Merck India), chloroform (Emplura, Merck India), ethanol (Absolute, Changshu Yangyuan, China) and methanol (Sigma Aldrich, ACS spectrophotometric grade, 98%) were used without further purification.

4.2 Synthesis methodologies

The synthesis of AISE QDs was performed by following a literature reported method with slight modifications.[30]

4.2.1 Preparation of selenium stock solution. 1 mmol Se powder, 1 mL oleylamine and 1 mL dodecane thiol were taken in a round bottomed flask followed by evacuation and refilling with N$_2$ three times at room temperature. Then the mixture was stirred under N$_2$ to dissolve the Se powder.

4.2.2 Synthesis of AISE QDs. In a separate three neck round bottomed flask, 0.5 mmol AgNO$_3$, 0.5 mmol InCl$_3$·4H$_2$O, 12 mL octadecene and 6 mL of oleylamine were loaded and cycled between vacuum and N$_2$ three times at 60 °C. Then, the mixture was heated to 88 °C. When the target temperature was achieved, 2 mL of Se stock solution was rapidly injected into it. The solution immediately turned dark brown. The mixture was again heated to 180 °C for QD-growth and aged at this temperature for 5 min. Finally, the reaction was quenched in a water bath and the product was isolated by precipitation with ethanol followed by centrifugation at 6500 rpm. The QDs were redispersed in chloroform for further use.

4.2.3 Synthesis of ZAISE QDs. 0.5 mmol AgNO$_3$, 0.5 mmol InCl$_3$·4H$_2$O and Zn(OAC)$_2$·2H$_2$O (varied from 0.02 to 0.06 mmol) were loaded into a three-neck round bottomed flask along with 6 mL of oleylamine and 12 mL of octadecene. The reaction mixture was cycled between vacuum and N$_2$ three times at 60 °C. Then, the mixture was heated to 88 °C. When the temperature reached 85 °C, the transparent colorless solution turned milky white. Then, 2 mL of Se-precursor solution was quickly injected into the above mentioned solution at 88 °C. The solution immediately turned dark brown and the mixture was further heated to 180 °C and kept at this temperature for 5 min. Finally, the reaction mixture was quenched in a water bath and the mixture was precipitated with ethanol followed by centrifugation. Finally the ZAISE QDs were redispersed in CHCl$_3$ and stored in the dark for further use.

4.2.4 Preparation of water soluble MPA-capped AISE and ZAISE QDs. The water soluble AISE and ZAISE QDs were prepared by replacing the initial hydrophobic oleylamine group with MPA. At first, 500 μL MPA was taken into a vial along with 4 mL MeOH and 1 mL distilled water. The pH of this solution was adjusted to 12 with 5 M NaOH. 0.5 mmol of AISE QDs dispersed into chloroform was taken into a separate vial and MPA-methanol solution was added to it followed by stirring for 4 h. Post stirring, the mixture was allowed to stand for few minutes to separate the phases. The bottom organic layer was discarded. The upper aqueous layer containing the QDs was washed with acetone to remove free MPA molecules and QDs were redispersed in 6 mL water for further use.

4.2.5 Synthesis of Cu$_x$S nanostructures. Cu$_x$S nanostructures were synthesized by following our previously reported method.[32] 5 mmol Cu(NO$_3$)$_2$·6H$_2$O and 5 mmol sulfur powder in 100 mL ethylene glycol were taken in a round bottomed flask and irradiated in a microwave chamber at 125 °C for 12 min at 600 W. The color of the solution changed from blue to deep green and a black colored product was precipitated. Finally, the product was washed with ethanol by centrifugation at 5000 rpm for 5 min and dried at 80 °C for 1 h to obtain the Cu$_x$S nanostructures.

4.3 Fabrication of QDSSCs

4.3.1 Preparation of the TiO$_2$ photoanode. FTO coated glass (Solaronix, TCO 22-7, 2.2 mm thickness) pieces were cleaned ultrasonically with soap water followed by distilled water and ethanol. Three different layers of TiO$_2$ were sequentially deposited onto the FTO glasses. At first, a compact layer was deposited by immersing the cleaned glasses into an aqueous solution of 40 mM TiCl$_4$ at 80 °C for 45 min followed by washing with distilled water and ethanol. Active and scattering layers were deposited by the doctor blade technique. The active layer was prepared on top of the compact layer by using a TiO$_2$ paste (Solaronix, Ti-Nanoxide T/SP, particle size ∼20 nm) followed by annealing at 500 °C in air for 1 h in a furnace (film thickness ∼10 μm). A ∼4 μm thick scattering layer of TiO$_2$ (Solaronix, Ti-Nanoxide R/SP, particle size ∼100 nm) was then coated on the active layer followed by annealing at 500 °C for another 1 h.

4.3.2 Sensitization of the TiO$_2$ photoanode. MPA-capped QDs were dispersed into 6 mL deionized water. 53 μL of MPA was added to the dispersion and the pH was maintained at 12 with 5 M NaOH. The TiO$_2$ films were dipped into this solution for sensitization and kept for 24 h. Finally, the QD sensitized TiO$_2$ films were washed with distilled water and kept for further use.

4.3.3 Preparation of the ZnS passivation layer. To passivate the QD layer, a very thin layer of ZnS was employed onto the QD deposited TiO$_2$ films by SILAR. At first, the QD-deposited TiO$_2$ photoanode was dipped into an aqueous solution of 0.1 M Zn(NO$_3$)$_2$·6H$_2$O solution for 1 min followed by rinsing with distilled water. The electrodes were further dipped into 0.1 M Na$_2$S·9H$_2$O solution for another 1 min. The electrodes were further rinsed with distilled water to remove the unbound S^{2-} ions. The protocol was repeated to achieve the desired number of SILAR cycles.

4.3.4 Preparation of TiO$_2$ and SiO$_2$ double passivation layers. Amorphous TiO$_2$ and SiO$_2$ double passivation layers were prepared by following the literature reported method.[34,35] At

first, the QDSSCs before ZnS treatment were dipped into 10 mM aqueous solution of $TiCl_4$ and kept at 40 °C for 30 min to create a very thin layer of amorphous TiO_2 over the QD deposited TiO_2 photoanode. Then the films were washed with distilled water followed by ethanol. Thereafter the ZnS passivation layer was applied as per the above protocol followed by rinsing with distilled water. These films were further immersed into an ethanolic solution of tetraethyl orthosilicate and kept for 2 h. Finally the electrodes were washed with ethanol for further use.

4.3.5 Preparation of the Cu_xS counter electrode. A paste of Cu_xS was prepared by stirring overnight a mixture of Cu_xS nanostructures and polyvinyledene fluoride (10 : 1 w/w) in N-methyl 2-pyrrolidone. The paste was doctor bladed on pre-cleaned FTO, dried and annealed at 80 °C for 1.5 h.

4.3.6 Electrolyte. A mixture of 2 M Na_2S, 2 M S and 0.2 M KCl solutions in methanol/H_2O (3 : 7 v/v) was employed as the electrolyte.

4.3.7 Preparation of QDSSCs. The QDSSCs were prepared by assembling the counter electrode and the QD-sensitized photoanode using a 50 μm thick parafilm spacer in a sandwich configuration. A 50 μL droplet of the polysulfide electrolyte was employed between the two electrodes before assembling them. The active area was selected by employing a mask onto the working electrodes. The active area of the electrode was 0.23 cm^2.

4.4 Characterization

The XRD measurements were carried out with a Rigaku powder X-ray diffractometer having Cu Kα = 1.54059 Å radiation. The ICP-MS measurements were performed by using a Thermo Scientific X-series using Plasma lab software. TEM images were obtained with a UHR-FEG TEM system (JEOL, Model JEM 2100 F) using a 200 kV electron source equipped with an energy dispersive X-ray spectroscope. To record the TEM images, EDAX and elemental mapping, the QD-sensitized photoanode with different inorganic coatings was crushed to powder and dispersed in isopropanol. UV-Vis absorbance spectra of the QD dispersion and the TiO_2 photoanode were recorded using a Jasco V-670 spectrophotometer. To record the absorbance spectra of the TiO_2 photoanode, the spectrophotometer was equipped with an integrating sphere. Room temperature PL spectra were measured with a Horiba Jobin Yvon Fluorolog using a Xe lamp as the excitation source with an excitation wavelength of 480 nm. The fluorescence lifetimes were recorded by using a time correlated single-photon counting spectrofluorimeter from HORIBA Jobin Yvon IBH. The fluorescence life time was calculated by fitting the decay curves by using an iterative fitting program provided by IBH. Photovoltaic measurements were carried out by using a solar simulator provided by Newport using a 300 W xenon lamp as a light source. The intensity of the light was adjusted to 100 mW cm^{-2} by using a reference silicon solar cell in the presence of a 1.5 G filter. The photovoltaic and the impedance measurements were carried out by using a CHI Electrochemical workstation. The plots were analyzed with inbuilt software in the electrochemical workstation.

Notes and references

1 M. C. Beard, *J. Phys. Chem. Lett.*, 2011, **2**, 1282–1288.
2 A. Sahasrabudhe and S. Bhattacharyya, *Chem. Mater.*, 2015, **27**, 4848–4859.
3 O. E. Semonin, J. M. Luther, S. Choi, H.-Y. Chen, J. Gao, A. J. Nozik and M. C. Beard, *Science*, 2011, **334**, 1530–1533.
4 A. J. Nozik, *Chem. Phys. Lett.*, 2008, **457**, 3–11.
5 P. V. Kamat, *Acc. Chem. Res.*, 2012, **45**, 1906–1915.
6 P. V. Kamat, *J. Phys. Chem. C*, 2007, **111**, 2834–2860.
7 Z. Pan, K. Zhao, J. Wang, H. Zhang, Y. Feng and X. Zhong, *ACS Nano*, 2013, **7**, 5215–5222.
8 Z. Pan, I. Mora-Seró, Q. Shen, H. Zhang, Y. Li, K. Zhao, J. Wang, X. Zhong and J. Bisquert, *J. Am. Chem. Soc.*, 2014, **136**, 9203–9210.
9 W. Li, Z. Pan and X. Zhong, *J. Mater. Chem. A*, 2015, **3**, 1649–1655.
10 K. P. Kadlag, P. Patil, M. J. Rao, S. Datta and A. Nag, *CrystEngComm*, 2014, **16**, 3605–3612.
11 M. G. Panthani, C. J. Stolle, D. K. Reid, D. J. Rhee, T. B. Harvey, V. A. Akhavan, Y. Yu and B. A. Korgel, *J. Phys. Chem. Lett.*, 2013, **4**, 2030–2034.
12 G. Halder and S. Bhattacharyya, *J. Phys. Chem. C*, 2015, **119**, 13404–13412.
13 J. Krustok, J. Raudoja, M. Krunks, H. Mändar and H. Collan, *J. Appl. Phys.*, 2000, **88**, 205–209.
14 B. Mao, C.-H. Chuang, F. Lu, L. Sang, J. Zhu and C. Burda, *J. Phys. Chem. C*, 2013, **117**, 648–656.
15 R. Bose, G. Manna, S. Jana and N. Pradhan, *Chem. Commun.*, 2014, **50**, 3074–3077.
16 M. Jagadeeswararao, A. Swarnkar, G. B. Markad and A. Nag, *J. Phys. Chem. C*, 2016, **120**, 19461–19469.
17 Y. Wang, Q. Zhang, Y. Li and H. Wang, *Nanoscale*, 2015, **7**, 6185–6192.
18 J. Han, Z. Liu, K. Guo, J. Ya, Y. Zhao, X. Zhang, T. Hong and J. Liu, *ACS Appl. Mater. Interfaces*, 2014, **6**, 17119–17125.
19 D. Aldakov, A. Lefrançois and P. Reiss, *J. Mater. Chem. C*, 2013, **1**, 3756–3776.
20 G. Hodes, *J. Phys. Chem. C*, 2008, **112**, 17778–17787.
21 H. McDaniel, N. Fuke, N. S. Makarov, J. M. Pietryga and V. I. Klimov, *Nat. Commun.*, 2013, **4**, 2887.
22 A. Guchhait and A. J. Pal, *ACS Appl. Mater. Interfaces*, 2013, **5**, 4181–4189.
23 A. G. Pattantyus-Abraham, I. J. Kramer, A. R. Barkhouse, X. Wang, G. Konstantatos, R. Debnath, L. Levina, I. Raabe,

11754 | *J. Mater. Chem. A*, 2017, **5**, 11746–11755

This journal is © The Royal Society of Chemistry 2017

M. K. Nazeeruddin, M. Grätzel and E. H. Sargent, *ACS Nano*, 2010, **4**, 3374–3380.

24 J. Du, Z. Du, J.-S. Hu, Z. Pan, Q. Shen, J. Sun, D. Long, H. Dong, L. Sun, X. Zhong and L.-J. Wan, *J. Am. Chem. Soc.*, 2016, **138**, 4201–4209.

25 M. A. Ahmed, K. E.-S. Rady, K. M. El-Shokrofy, A. A. Arais and M. S. Shams, *Mater. Sci. Appl.*, 2014, **5**, 932–942.

26 J. E. Jaffe and A. Zunger, *Phys. Rev. B: Condens. Matter*, 1984, **29**, 1882.

27 A. R. Kirmani, A. Kiani, M. M. Said, O. Voznyy, N. Wehbe, G. Walters, S. Barlow, E. H. Sargent, S. R. Marder and A. Amassian, *ACS Energy Lett.*, 2016, **1**, 922–930.

28 X. Tang, W. B. A. Ho and J. M. Xue, *J. Phys. Chem. C*, 2012, **116**, 9769–9773.

29 B. Chen, H. Zhong, W. Zhang, Z. Tan, Y. Li, C. Yu, T. Zhai, Y. Bando, S. Yang and B. Zou, *Adv. Funct. Mater.*, 2012, **22**, 2081–2088.

30 D. Yao, H. Liu, Y. Liu, C. Dong, K. Zhang, Y. Sheng, J. Cui, H. Zhang and B. Yang, *Nanoscale*, 2015, **7**, 18570–18578.

31 B. Mao, C.-H. Chuang, J. Wang and C. Burda, *J. Phys. Chem. C*, 2011, **115**, 8945–8954.

32 D. Ghosh, G. Halder, A. Sahasrabudhe and S. Bhattacharyya, *Nanoscale*, 2016, **8**, 10632–10641.

33 A. Sahasrabudhe, S. Kapri and S. Bhattacharyya, *Carbon*, 2016, **107**, 395–404.

34 Z. Ren, J. Wang, Z. Pan, K. Zhao, H. Zhang, Y. Li, Y. Zhao, I. Mora-Sero, J. Bisquert and X. Zhong, *Chem. Mater.*, 2015, **27**, 8398–8405.

35 K. Zhao, Z. Pan, I. Mora-Seró, E. Cánovas, H. Wang, Y. Song, X. Gong, J. Wang, M. Bonn, J. Bisquert and X. Zhong, *J. Am. Chem. Soc.*, 2015, **137**, 5602–5609.

36 J.-Y. Kim, J. Yang, J. H. Yu, W. Baek, C.-H. Lee, H. J. Son, T. Hyeon and M. J. Ko, *ACS Nano*, 2015, **9**, 11286–11295.

37 J. Tian and G. Cao, *J. Phys. Chem. Lett.*, 2015, **6**, 1859–1869.

38 K. Zhao, Z. Pan and X. Zhong, *J. Phys. Chem. Lett.*, 2016, **7**, 406–417.

39 N. Guijarro, J. M. Campiña, Q. Shen, T. Toyoda, T. Lana-Villarreal and R. Gómez, *Phys. Chem. Chem. Phys.*, 2011, **13**, 12024–12032.

40 Z. Liu, M. Miyauchi, Y. Uemura, Y. Cui, K. Hara, Z. Zhao, K. Sunahara and A. Furube, *Appl. Phys. Lett.*, 2010, **96**, 233107.

41 Z. Ren, Z. Wang, R. Wang, Z. Pan, X. Gong and X. Zhong, *Chem. Mater.*, 2016, **28**, 2323–2330.

42 Z. Pan and X. Zhong, *J. Mater. Chem. A*, 2016, **4**, 18976–18982.

43 T. Kameyama, Y. Douke, H. Shibakawa, M. Kawaraya, H. Segawa, S. Kuwabata and T. Torimoto, *J. Phys. Chem. C*, 2014, **118**, 29517–29524.

44 S. M. Kobosko, D. H. Jara and P. V. Kamat, *ACS Appl. Mater. Interfaces*, DOI: 10.1021/acsami.6b14604.

45 C. Cai, L. Zhai, Y. Ma, C. Zou, L. Zhang, Y. Yang and S. Huang, *J. Power Sources*, 2017, **341**, 11–18.

This journal is © The Royal Society of Chemistry 2017

J. Mater. Chem. A, 2017, **5**, 11746–11755 | **11755**